PNAS RESEARCH ARTICLE | EARTH, ATMOSPHERIC, AND PLANETARY SCIENCES

Hematite U-Pb dating of Snowball Earth meltwater events

Liam Courtney-Davies[a,1], Rebecca M. Flowers[a], Christine S. Siddoway[b], Adrian Tasistro-Hart[c], and Francis A. Macdonald[d]

Affiliations are included on p. 9.

Edited by Dennis Kent, Columbia University, Palisades, NY; received June 6, 2024; accepted October 8, 2024

The Snowball Earth hypothesis predicts global ice cover; however, previous descriptions of Cryogenian (720-635 Ma) glacial deposits are limited to continental margins and shallow marine basins. The Tavakaiv (Tava) sandstone injectites and ridges in Colorado, USA, preserve a rare terrestrial record of Cryogenian low-latitude glaciation. Injectites, ridges, and chemically weathered crystalline rock display features characteristic of fluidization and pervasive deformation in a subglacial environment due to glacial loading, fluid overpressure, and repeated sand injection during meltwater events. In situ hematite U-Pb geochronology on hematite-quartz veins, which crosscut and are cut by Tava dikes, constrain sand injection at ~690-660 Ma. We attribute early Tava sand injection episodes to basal melting associated with rifting and geothermal heating, and later injections to meltwater generation during ~661 Ma Sturtian deglaciation. A modern analog is provided by the Ross Embayment of Antarctica, where rift-related faults border sediment-filled basins, overpressurized fluids circulate in confined aquifers below ice, and extensive preglacial topography is preserved. Field evidence and geochronology in Colorado further highlight that deep chemical weathering of Proterozoic bedrock and denudation associated with the Great Unconformity predate Cryogenian injection of fluidized sand, consistent with limited glacial erosion.

Snowball Earth | Sturtian glaciation | hematite U-Pb | injectites | great unconformity

Significance

Terrestrial records of the Cryogenian ice sheets are rare, but provide constraints on low-latitude glacial processes, including glacial erosion, and climate models of Snowball Earth. Here, we document a terrestrial glacial record in the form of sandstone dikes (injectites) and ridges, which preserve features characteristic of fluidization and deformation in a subglacial environment. We use in situ hematite U-Pb geochronology to date injectite formation, providing constraints on glacial meltwater events associated with rifting and deglaciation. The chemically weathered crystalline rock associated with the sandstones lacks evidence of mechanical abrasion and glacial scouring, suggesting that erosion at the Great Unconformity predates the Sturtian glaciation.

Energy balance climate models display a bifurcation when ice-sheet growth passes a critical latitude threshold, due to the high albedo of ice relative to seawater, which leads to a runaway ice-albedo feedback or Snowball Earth (1). The theory of Snowball Earth climate state was developed from energy balance models of ocean albedo, in the manner that Plate Tectonics originated as a theory for ocean basins. Geological records of low-latitude Cryogenian (720-635 Ma) glaciation are documented along continental margins and shallow marine basins, but the degree to which ice covered the continents during Snowball Earth is poorly constrained and inferred primarily from climate models (1–5).

Knowledge of the extent of Cryogenian continental glaciation is acknowledged as essential for understanding sea-level change, climate dynamics, albedo, dust generation, and terrestrial habitability during Snowball events (6). On the western continental margin of North America, striated clasts in Cryogenian diamictites (720-635 Ma) demonstrate the presence of at least some grounded ice (e.g., refs. 7–9). Climate models predict that sublimation should have exceeded precipitation at low latitudes (2), suggesting that dry valleys may have also existed in the continental interior of North America, perforating the cover of continental ice. However, the dynamics of these ice sheets, and whether ice-flow would rapidly cover zones of sublimation and erode underlying bedrock, is unknown. For example, it was recently proposed that large ice sheets eroded kilometers of rock from continental interiors to subduction zones to form the Great Unconformity (10–12), but geological constraints on the extent and dynamics of continental ice during a Snowball Earth are lacking.

Here, we characterize and date the formation of continental interior Cryogenian Snowball Earth deposits. Neoproterozoic clastic dikes and sandstone ridges of the Colorado Front Range, USA [Fig. 1; (13, 14)], informally named Tavakaiv sandstone (or Tava), are hosted by ca. 1720–1070 Ma gneiss and granites. Tava injectites consist of structureless, granule- to cobble-bearing, quartzose sandstone that locally suspends angular intraclasts [Fig. 2 and *SI Appendix*, Figs. S1–S3; (13, 14)]. Larger Tava bodies, termed sandstone ridges, are a constituent of the Proterozoic basement, and of sufficient scale to appear on geologic quadrangle maps of the region [(15–17); Fig. 1 and *SI Appendix*, Fig. S2)].

Previous research used the near-surface emplacement into weathered and fractured basement inferred for the Tava dikes (13, 14), as well as hematite (U-Th)/He dates of 676 ± 26 Ma (19), as evidence that the Proterozoic basement of the southern Front Range was exhumed to the surface prior to the Cryogenian glaciations (14). Additionally, Tava detrital zircon spectra and trace element geochemistry indicate a proximal source for ca. 1700

Author contributions: L.C.-D., R.M.F., C.S.S., and F.A.M. designed research; L.C.-D., R.M.F., C.S.S., A.T.-H., and F.A.M. performed research; L.C.-D., R.M.F., C.S.S., A.T.-H., and F.A.M. contributed new reagents/analytic tools; L.C.-D., R.M.F., C.S.S., A.T.-H., and F.A.M. analyzed data; and L.C.-D., R.M.F., C.S.S., A.T.-H., and F.A.M. wrote the paper.

The authors declare no competing interest.

This article is a PNAS Direct Submission.

[1]To whom correspondence may be addressed. Email: liam.courtney-davies@colorado.edu.

This article contains supporting information online at https://www.pnas.org/lookup/suppl/doi:10.1073/pnas.2410759121/-/DCSupplemental.

Published November 11, 2024.

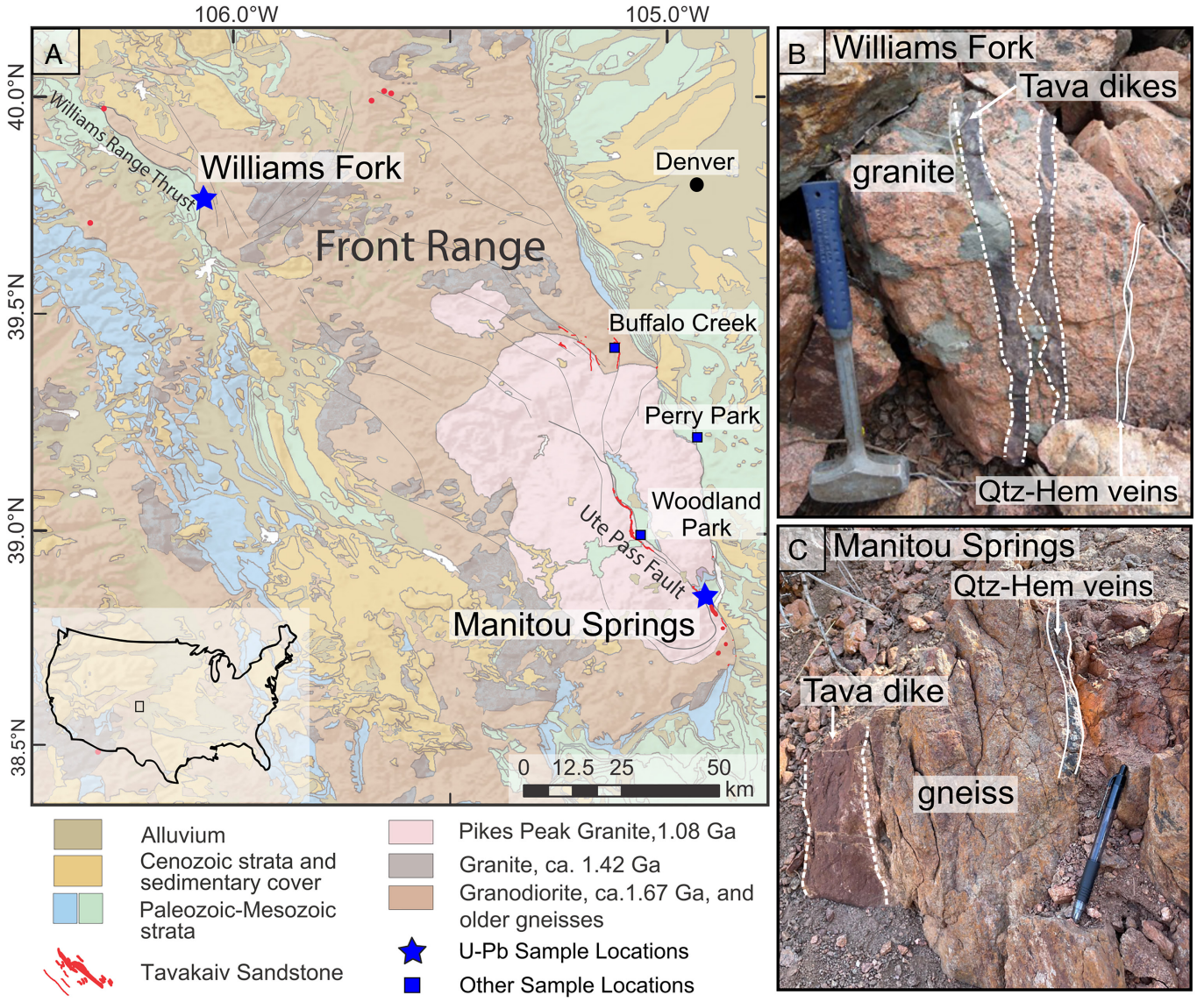

Fig. 1. Map of study area and photographs of rock outcrops. (*A*) Geological map of the southern Front Range in Colorado with Tava outcrop and sample localities marked. (*B* and *C*) Photographs displaying relationships between Proterozoic host rocks, Tava injectites, and hematite-quartz veins at the two sample localities. These sites are complementary as hematite veins are best developed in the Williams Fork Range, and sedimentary structures are better developed at Manitou Springs, possibly due to different depths of exposure at the two sites. Therefore, we use these sites to assemble a composite view of coeval sedimentation and mineralization processes.

and 1075 Ma grains (19–22), which suggests that the local basement was at the surface before Tava dike injection to serve as a source for Tava detritus. However, (12) argued that the Tava sandstone may be older than the hematite (U-Th)/He results, that the sandstone's origins are too enigmatic for the Tava to be used as a near-surface marker, and that the basement was not initially exhumed to form the Great Unconformity erosion surface until multikilometer erosion during Snowball Earth. The He closure temperature for multidomain diffusion in hematite is between ~0 to 150 °C depending on crystallite size (23), such that He in hematite is amenable to resetting and the (U-Th)/He dates could record a postcrystallization cooling age, and thus not date the time of hematite crystallization nor Tava injection (12, 13).

To circumvent the issue of resetting of lower temperature thermochronometers like He in hematite, radiometric systems with higher closure temperatures for the daughter products such as U-Pb can be used to define the time of mineral crystallization more accurately. Hematite can incorporate U into its crystal lattice at up to wt. % concentrations and it retains U and Pb over geologic timescales (24, 25). Hematite with these attributes provides a means to date hydrothermal fluids precipitated in faults and veins with complex histories or resulting from fluid–rock interactions over prolonged intervals (e.g., refs. 25–27). There are no direct constraints on the closure (resetting) temperature of the U-Pb system in hematite, but it is expected to be akin to magnetite based on related crystal structures [magnetite Pb closure T ~550 °C; (28)] and indirect evidence whereby hematite retains primary U-Pb systematics in long-lived high-T hydrothermal environments (29, 30).

Here, we present field evidence indicating a subglacial origin of the Tava sandstone, with particular focus on the extensive Tava sandstone ridges and soft-sediment deformation structures. Guided by these observations, we selected two study sites for in situ hematite U-Pb geochronology to better resolve the age and origin of the Tava sandstone. Although the two Tava sites are separated by ~125 km and are hosted by different lithologies (Fig. 1*A*), they share common sedimentary structures and hydrothermal features including hematite veins intimately associated with Tava dikes (Fig. 1 *B* and *C*). We deployed the high spatial

resolution of laser ablation-inductively coupled plasma-mass spectrometry (LA-ICP-MS) to target microscale mutually crosscutting relationships between Tava and hematite veins. Together, these data constrain discrete glacial meltwater events, reveal dynamic interactions between large volumes of fluidized supracrustal sediments and underlying basement, and limit the amount of glacial erosion that could have occurred along the Great Unconformity.

Tava Sandstone Field Relationships

The most extensive exposures of Tava sandstone ridges and dikes border the Ute Pass Fault (Fig. 1*A*). Four dike occurrences are proximal to the Great Unconformity, and dikes are documented in at least ten locations in Colorado other than the Ute Pass Fault zone (19).

Sandstone Ridges. Well-indurated sandstone forms prominent elongate ridges that align with strands of the Ute Pass Fault in Manitou Springs (16) and northwest of Manitou Springs [(15, 17); Fig. 2 *A* and *B* and *SI Appendix*, Fig. S4). At the Manitou Springs hematite U-Pb sample site, as well as at other sandstone ridge locations, the sandstone is fine- to coarse-grained, massive, structureless quartz arenite, containing granule- to pebble-sized clasts of rounded to subrounded polycrystalline quartz and minor granite (Fig. 1). Sorting and grading are weak to absent, such that larger grains are nontouching and supported by a very poorly

Fig. 2. (*A* and *B*) Aerial images of Tava injectites. (*A*) Aerial drone photomosaic showing a prominent light-colored Tava sill, 70 to 90 cm thick (the prominent rock band), hosted by mottled Tava siliciclastics of a sandstone ridge. The deformed sill appears as a tight, asymmetrical, E-vergent fold, reverse faulted along the middle limb. Geologist for scale. View is to North North East. (*B*) Stack of recumbent ptygmatic folds affecting one or multiple sills injected into a sandstone ridge. Aerial oblique view, captured by drone survey, is to the North. The nonsystematic folds are broken and discontinuous, interrupted by short faults, or "slides" (cf. ref. 18) that are partially obscured by slope debris. (*C*) Three Tava injectites within a meter-wide composite dike. Earlier-injected light purple-gray and red-brown portions (labeled 1, 2) and a large fragment of granite wallrock (label g) were brecciated and crosscut by white sand injectite (labeled 3) that suspends angular clasts and forms mm-scale dikelets across clasts and early dikes. The features are indicative of hydraulic brecciation of an existing sandstone dike by fluidized sand that now appears as pale matrix surrounding rotated fragments and a wallrock clast, and as crosscutting dikelets. (*D*) Photograph of an outcrop displaying multiple generations of Tava injectite within a granite host within North Cheyenne Cañon. (*E*) Meter-wide dyke with matrix-supported clasts concentrated along dyke margin.

sorted rounded to subrounded fine- to medium-grained matrix. Ridges along the Ute Pass Fault zone reach or exceed 900 m in length, 250 m width, and 150 m of relief (e.g., ref. 13; *SI Appendix*, Fig. S4). The contacts on the margins of sandstone bodies are poorly exposed due to deep weathering of the neighboring granites and/or presence of angular, broken sandstone blocks upon steep slopes, however throughgoing sandstone dikes are observed to cross from crystalline host rock into sand ridges. The ridges display nonsystematic internal structures, including: i) subunits that display differences in grain size, type of cement, and degree of induration (31); ii) semiplanar partings suggestive of bedding breaks that pass into structureless sandstone (33); and iii) cross-cutting sandstone dikes and sills (13, 32) that are folded and/or faulted (Fig. 2 and *SI Appendix*, Fig. S3). Where semiplanar partings are observed, these have been rendered on published geological maps as bedding (e.g. refs. 15 and 16), but close examination of the sandstone reveals no sorting or bedforms. The parting surfaces themselves may be grooved or delicately striated with slicken surfaces, so the breaks may be "pseudobedding" imparted by shearing (see ref. 33, for an Ordovician analog). The Tava sandstone's typical color is deep red to pale purple, but white, faintly green, or pale-yellow hues are also common. The darker-colored sandstone commonly displays light color mottling (*SI Appendix*, Fig. S3*C*).

Sedimentary Injectites. The injectites consist of fine- to coarse-grained, rounded to subrounded quartz sand, with accessory minerals <3% (*SI Appendix*, Fig. S1). An earlier generation of dikes generally is purple to maroon in color, well-indurated, and locally mottled (Figs. 1*C* and 2 *C* and *D* and *SI Appendix*, Fig. S5 *A*–*D*). A successive generation is light-colored white, tan, or pale-yellow (*SI Appendix*, Figs. S3 and S7*A*). Dikes contain dispersed granules, pebbles, (*SI Appendix*, Fig. S1 *B* and *C*) and rare cobbles of quartz (up to 7 cm in length). Elongate, angular fragments of the host granite may be present, with the long dimension of such clasts (0.1 to >15 cm in length) commonly displaying a "jigsaw" arrangement (14). Elsewhere, thin flakes of granite are imbricated or "jammed" in constrictions or narrow apophyses, with clay intraclasts also present.

Dikes have planar to "stepped" margins, vertical to subvertical geometry, and thickness ranging from 2 mm to >1 m. Injectites with stepped margins are marked by abrupt changes in thickness ("jack up" structure; (18)). Some dikes display diffuse grading parallel to margins, with pebbles preferentially concentrated along one margin (*SI Appendix*, Fig. S1*C*). Horizontal injectite sills, 0.1 to 1.0 m-thick, are also present (*SI Appendix*, Figs. S1 and S3 *C* and *D*). Some low-angle dikes display apophyses, which provide an indication of change in stress state during injection (34). Younger, light-colored injectites locally contain angular blocks of earlier-formed purple or red injectites (Fig. 2*C*).

Clastic dikes intruding both crystalline rock (Fig. 2 *C*–*E* and *SI Appendix*, Figs. S5*B* and S6 *A*–*D*) and Tava sandstone ridges (Fig. 2 *A* and *B* and *SI Appendix*, Fig. S3 *C* and *D*) are deformed by inclined and recumbent imbricate folds, and reverse-faults. The geometries of folds of dikes are nonsystematic, in that fold shapes and axis trends vary. Fold forms vary from gentle and upright to isoclinal, recumbent, and ptygmatic (Fig. 2 *A* and *B* and *SI Appendix*, Figs. S3 *C* and *D*, S5*B*, and S6 *A*–*D*). Light-colored Tava injectites cut red to purple, earlier-emplaced injectite and ridge sandstone, and locally contain dark, angular intraclasts of the older Tava rock (Fig. 2*C* and *SI Appendix*, Fig. S3). "Conglomeratic" injectites contain imbricated, ruptured pebbles (*SI Appendix*, Fig S6 *H* and *I*).

Fault Associations for Sample Localities. At both sample locations, the Tava sandstone is associated with–and likely owes its preservation to–polyphase faults. At Manitou Springs, the high-angle Ute Pass Fault (Fig. 1*A* and *SI Appendix*, Fig. S2) is an element within the Rocky Mountain Front, a longstanding crustal boundary established at 1.4 to 1.1 Ga and reactivated during Neoproterozoic rifting of the western margin of Laurentia (35). The Ute Pass Fault transects the Pikes Peak batholith and the Proterozoic structure may have played a role in the uplift and erosion of the granite, and burial of Tava situated in a footwall position. The fault was later reactivated during the Pennsylvanian Ancestral Rocky Mountain and Cretaceous Laramide orogenies (16, 36), during which Tava sandstone was eroded, as evidenced by Tava sandstone clasts within Pennsylvanian basal conglomerates and voluminous blocky Tava debris in unconsolidated alluvial terraces flanking the range front at Colorado Springs.

Tava injectites in the Williams Fork Range (*SI Appendix*, Fig. S5) occupy the thin leading edge of a Laramide thrust fault that (37) accommodated at least 9 km and as much as 20 km of westward translation (38). The injectites are situated above tree line in competent to deeply weathered Boulder Creek granodiorite bordering a Cenozoic extensional basin (39). Tectonic restoration of fault slip would place the Williams Fork Range occurrence along the trend of subvertical Tava injectites along the eastern Front Range (40, 41).

Hematite U-Pb Geochronology

Samples and Hematite Morphology. Although Tava dikes outcrop at numerous locations in the Colorado Front Range (Fig. 1*A*), only a few sites contain both injectites and hematite-quartz veins in close spatial and crosscutting relationships. Of seven samples dated in this study, six are from above tree line in the Williams Fork Range (Fig. 1 *A* and *B* and *SI Appendix*, Fig. S5), where crosscutting relationships between Tava dikes and veins are best defined. The final sample (Fig. 1*C*) is from the Sutherland Creek drainage near Manitou Springs, where excellent exposures of a sandstone ridge (*SI Appendix*, Fig. S4*B*) are cut by multiple generations of deformed dikes (Fig. 2 *A* and *B* and *SI Appendix*, Fig. S3 *C* and *D*).

The host rock at the Williams Fork locality is weathered ~1.7 Ga Boulder Creek granodiorite (37, 41). Here, Tava dikes are mm- to cm- scale in width and are near-ubiquitously associated with hematite-quartz veins. The veins crosscut Tava dikes, rim the dikes, or cut through granodiorite proximal to Tava dikes (*SI Appendix*, Fig. S5). The fine scale of the dikes and veins, and the extent of weathering of host rock, obscure outcrop-scale relationships, but spatial and cross-cutting relationships are readily visible within hand specimens and photomicrographs (Fig. 3 and *SI Appendix*, Fig. S9). The Tava dikes contain intraclasts of host granite and older Tava sandstone. In some instances, injected pebbly sand of the Tava broke and entrained preexisting vein quartz (*SI Appendix*, Fig. S5*E*). Hematite from veins associated with Tava dikes was previously dated at this location by Jensen et al. (19) using (U-Th)/He.

In exposures bordering Sutherland Creek at the Manitou Springs locality, Tava dikes intrude a sandstone ridge and Proterozoic gneiss in a fault-bounded block that was transported (*SI Appendix*, Figs. S2 and S4*B*; transferred from the Ute Pass Fault hanging wall to footwall) after the Cretaceous Period (16, 32). In one exposure low on the slope, a deep red sandstone dike (10- to 12- cm wide) and a solitary vein of coarse hematite (width, 2-cm), run subparallel to each other over a distance of 22 cm (Fig. 1*C*). The relationship can be followed upslope, discontinuously, for >50 m. The injectite

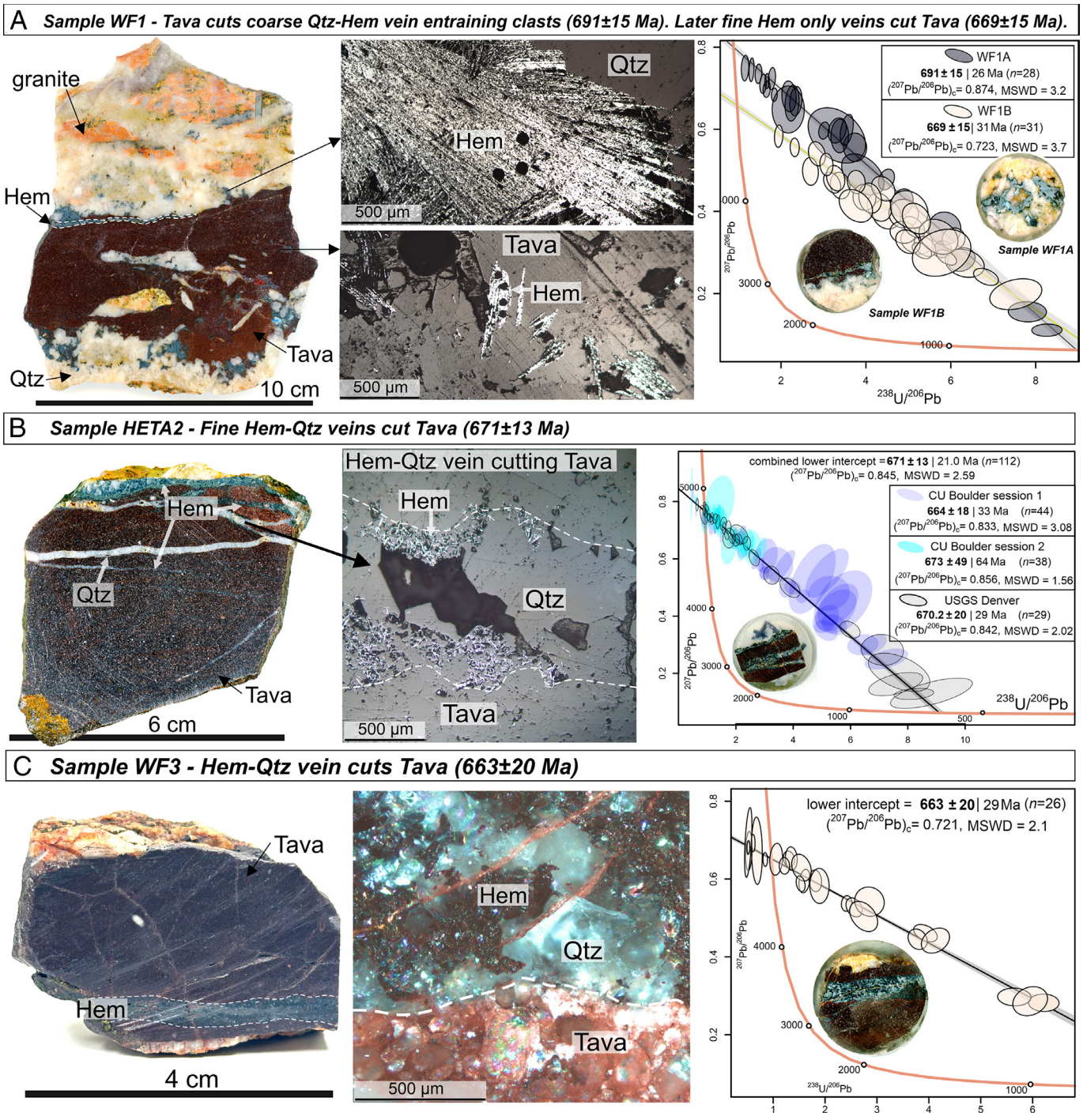

Fig. 3. Dated hematite and corresponding Tera-Wasserburg U-Pb diagrams for samples with well-defined cross-cutting relationships between hematite-quartz veins and Tava. Rock and reflected light images and corresponding 1-inch round polished block inserts within the Tera-Wasserburg diagrams for samples (*A*) WF1, (*B*) HETA2, and (*C*) WF3.

and hematite vein are observed to converge upslope, become obscured beneath a covered interval, and then reappear with hematite vein on the opposite side and within 2 cm of the margin of the sandstone dike in an exposure >3 m in length. From the similarity in outcrop appearance, structural orientation, and petrographic characteristics of the hematite vein in lower, middle, and upper parts of the slope, proximal to the Tava dike, we infer that the vein is continuous through the host gneiss, and the relationships are consistent with the Tava dike cutting the hematite vein. Elsewhere across the slope at this location, numerous hematite-free quartz veins are cut by Tava dikes and some contain Tava fragments.

Hematite grain sizes and textures vary between samples. In the host gneiss and in massive quartz veins not in contact with Tava, specular hematite forms radial splays of densely packed, tabular (platy) hematite crystals with distinct crystal boundaries up to ~1,200 µm in length. In contrast, hematite-bearing veins which rim, cut, or are cut by Tava contain smaller hematite formed as tabular plates generally <400 µm in length (*SI Appendix*, Fig S8*A*).

Hematite U-Pb Dating Results. U–Pb and trace element data were collected by LA–ICP–MS at the CU TRaIL (Thermochronology Research and Instrumentation Lab at the University of Colorado, Boulder). All U-Pb dates are presented as lower intercepts on

Tera-Wasserburg diagrams (Fig. 3 and *SI Appendix*, Fig. S8), with data points plotting along an intercept representing mixing between initial common Pb and ingrown radiogenic Pb. Isotopic ratio measurements are displayed as ellipses (at 2σ confidence) and intercept uncertainties at 2σ are reported as analytical, followed by +95% CI. Uncertainties related to standard measurement and measurement repeatability are propagated into uncertainties. The U-Pb dataset is reported in *SI Appendix*, Table S1. Laser ablation pits show well-defined crater walls and near flat bottoms (*SI Appendix*, Fig. S8*B*) with evidence of redeposition/melting similar to that observed in ref. 29. Pits are on average 19 μm deep, representing ~1,200 μm^3 of ablated material. Downhole ablation profiles for hematite consistently show smooth (flat) signals for all analyzed isotopes. An example profile from a typical hematite analysis in sample HETA2 is presented in *SI Appendix*, Fig S8*C*. Across 298 total LA-ICP-MS hematite analyses in this study, U, Th, and total Pb concentrations averaged 4.9, 3.0, and 8.5 ppm, respectively (*SI Appendix*, Fig S8*D*).

For each sample, Tera-Wasserburg diagrams are accompanied by rock and reflected light images to highlight the relationships between Tava and hematite veins. Fig. 3 includes images and data for the samples with the best-defined cross-cutting relationships between the Tava and dated hematite. *SI Appendix*, Fig. S9 includes the samples with more ambiguous relationships. Each sample and its geochronology are described below individually.

Two polished blocks were obtained from sample *WF1* (Fig. 3*A*). The first (WF1A) is composed of massive quartz with pockets of hematite plates filling spaces between quartz grains and yields a lower intercept date at 691 ± 15 Ma. The second (WF1B) is from a hematite vein at the interface between Tava and quartz and provides a younger 669 ± 15 Ma intercept. These two dates define a Tava injection window, as WF1A represents a preexisting hematite-quartz vein cut by Tava which also entrains hematite-quartz clasts, and WF1B comprises later, finer, hematite-only veinlets, which precipitate across Tava.

U-Pb data for sample *HETA2* were collected from the same polished block in two labs over three LA-ICP-MS sessions at CU Boulder and the USGS Denver to assess the repeatability of results (Fig. 3*B* and *SI Appendix*, Fig. S8). This sample contains both quartz and hematite-dominant veins which cut reddish Tava injectites. The lower intercept date for all three sessions is within uncertainty of one another, and when combined, produces an intercept at 671 ± 13 Ma. The poor precision of the second CU Boulder session is likely due to the low abundance of high-quality grains after two previous dating sessions without repolishing.

U-Pb data for four other samples were also acquired. Sample *WF3* (Fig. 3*C*) contains hematite-dominant veins cutting Tava which yield a lower intercept at 663 ± 20 Ma. The contact between red stained Tava and the hematite-quartz vein is sharp, with specks of red stained Tava quartz grains visible within the hematite-dominant vein. Sample *HETA4* (*SI Appendix*, Fig. S9*A*) contains multiple Tava generations distinguished by their distinct color, intruding into granite and rimmed by hematite-quartz veins, as well as cutting hematite veins. Datapoints are highly scattered, as reflected by the high MSWD. Several data points contain very high Th contents which is unusual for hematite and likely represent inclusions or sampling of mixed phases. When excluded, the remaining data points form an intercept at 675 ± 32 Ma. Sample *WF2* (*SI Appendix*, Fig. S9*B*) contains a vein comprising a hematite core surrounded by quartz, which is in turn rimmed by hematite and cutting through Tava. Data have a large spread but define a distinct intercept at 696 ± 10 Ma. Sample *MSIT-SH* (*SI Appendix*, Fig. S9*C*) is the sole sample from the Manitou Springs location. It comprises very coarse hematite plates from a vein paralleling a Tava dike hosted by gneiss. Precision is low but defines a lower intercept at 678 ± 41 Ma.

Dated samples' initial $^{207}Pb/^{206}Pb$ range between 0.874 and 0.721, representing minor variation for specimens containing such little U. One outlier exists (HETA4, *SI Appendix*, Fig. S9*A*), where initial $^{207}Pb/^{206}Pb$ intercepts at 0.554. This sample contains anomalously high Th (up to 25 ppm, compared to generally 0 to 1 ppm for all other samples). Both the anomalous initial $^{207}Pb/^{206}Pb$ and high Th may be due to late forming inclusions or a heterogenous fluid, contributing to increased scatter in data evident from a high MSWD of 12.

To summarize, U-Pb lower intercept dates from seven samples range between 696 ± 10 Ma and 663 ± 20 Ma. The most radiogenic samples (HETA2, WF1A, and WF2), form lower intercepts at 671 ± 13 Ma, 691 ± 15 Ma, and 696 ± 10 Ma, respectively. One of the seven samples has hematite entrained by Tava, thus providing a maximum age of 691 ± 15 Ma for that Tava dike (sample WF1A). Three samples have hematite-quartz veins cutting Tava, thus providing minimum ages of 669 ± 15 Ma, 671 ± 13 Ma, and 663 ± 20 Ma for those Tava dikes (samples WF1B, HETA2, WF3). Three samples that have hematite-quartz veins characterized by more ambiguous relationships with the Tava (samples HETA4, WF2, MSIT-SH) yield dates that overlap with the rest of the sample suite.

Discussion

Multiple Pulses of Tava Sand Injection at Shallow Depth during Sturtian Snowball Earth. Hematite veins across seven samples yield a range of intercept dates between 696 ± 10 Ma and 663 ± 20 Ma (Fig. 3 and *SI Appendix*, Fig. S9), overlapping with the 717-661 Ma Sturtian glaciation, both on Laurentia (42, and references therein) and globally (43). These results are consistent with crosscutting relationships at the outcrop, hand-sample, and microscopic scales that reveal multiple generations of both hematite-quartz veins and Tava dikes, with distinct Tava injectite generations that crosscut and are entrained within one another (Figs. 2 and 3 and *SI Appendix*, Figs. S3 and S9) (13). Combined, these data demonstrate repeated pulses of fluidized sand injection between ~690 and ~660 Ma. The age bracketing of a single Tava dike is best highlighted in Fig. 3*A* (sample WF1), where a hematite-quartz vein with large radial hematite crystals is dated at 691 ± 15 Ma. This vein is cut by a Tava dike that encapsulates fragments of the vein, and this Tava dike is then cut by very fine hematite-only veinlets, which yield a hematite U-Pb date of 669 ± 15 Ma. Therefore, this Tava dike must have been emplaced at some time between 691 ± 15 and 669 ± 15 Ma. Such dates are repeated throughout five other samples. These new U-Pb dates provide absolute timing for hematite precipitation and hence Tava emplacement, consistent with a 676 ± 26 Ma hematite (U-Th)/He date from the same location and confirming the previously interpreted Cryogenian injection age of the Tava (19).

Based on fluid inclusion studies at the Williams Fork location, hydrothermal Fe^{2+} bearing fluids precipitated hematite-bearing veins with estimated fluid temperatures of ~210 to 230 °C (19). Precipitation of metals from fluids requires physiochemical changes in the environment (e.g., T, pressure, pH, and redox potential). This implies shallow hematite precipitation of <3 km where oxygenated sources can penetrate, which is supported by relatively low fluid inclusion formation pressure estimates (19, 44), and the 0.5 km to ≤1 km depth limit for sand injection (34, 45, 46).

Evidence for Subglacial Sedimentary Origin of Tava Sandstone Bodies. A range of characteristics provides evidence for a subglacial origin of the Tava sandstone, with dike injection due

to overpressured meltwater. The massive Tava sandstone ridges lack bedding and bedforms on scales of 10 s to 100 s of meters. Sedimentary rocks with this characteristic (e.g., ref. 47) are not produced in marine, fluvial, or aeolian settings with a free surface boundary, and the scale and geometry of the sand ridges and injectites are inconsistent with formation as permafrost ice wedges (3, 48). Rather, the Tava ridges closely resemble sandstone ridges documented in Hirnantian terrestrial subglacial deposits of North Africa (49). The ridges in North Africa formed as glacial ice plowed and sculpted weakly lithified preglacial sandstone or subglacial esker sediments into ridges. They are pervaded by sandstone dikes (50) that represent hydrofracture arrays, an integral part of subglacial hydrogeological systems developed dynamically as conduits for overpressured water beneath ice-sheets (51).

Fluidization and traction of subglacial sediment modifies bedforms such as eskers and kames, creating sand or sandy till ridges (49) that commonly undergo further deformation due to ice–bed coupling (47). In the structureless sediment forming the sand ridges, injectites serve as essential markers for soft-sediment deformation (e.g., ref. 34). Fluid overpressure and fluidization in the Tava are demonstrated by the sedimentology (*SI Appendix*, Figs. S1 and S3) and lobate contacts (*SI Appendix*, Fig. S7 *C* and *D*) of some injectites, crosscutting relationships requiring multiple injection pulses (Fig. 2 *C* and *D* and *SI Appendix*, Fig. S3), and ptygmatically folded injectites that originated as subvertical dikes, later folded by glacio-tectonism (Fig. 2 *A* and *B*). Evidence of wholesale soft-sediment deformation includes isoclinal to inclined, disharmonic folds and faults (Fig. 2 *A* and *B*) imparted upon injectites within Tava sandstone ridges. We attribute deformation to the ice–bed coupling of saturated deposits beneath flowing ice (e.g., ref. 34). Tava injectites within incompetent weathered crystalline rock (*SI Appendix*, Figs. S5 *A* and *B* and S6 *A–D*) were similarly deformed, providing evidence that the entire substrate was fluidized (e.g. refs. 18, 52, and 53). Comparable ptygmatically folded sand injectites are described in the Permo-Carboniferous Dwyka tillite of South Africa (34).

Features of Tava sandstone that indicate fluidization and deformation, likely achieved due to generation of meltwater, include sand injectite dikes and sills (34, 54), so numerous as to constitute a "swarm" (*SI Appendix*, Fig. S3); the near-absence of sorting and bedding in dikes and sand ridges [*SI Appendix*, Fig. S1 *A–C*; (55)]; fluted and lobate dike contacts [*SI Appendix*, Figs. S1*D* and S7 *C* and *D*; (35)]; diffuse concentration of pebbles parallel to one dike margin [*SI Appendix*, Fig. S1*C*; (56)] and diffuse injectite margins [*SI Appendix*, Fig. S7*D*; (57)]; and sills with stepped margins that display abrupt changes in thickness and jigsaw arrangements of wallrock intraclasts (58), including older Tava sandstone within younger Tava injectites [Fig. 2*C*; (13)]. Such relationships are known from subglacial environments and provide clear evidence of successive pulses of fluid overpressure and sedimentary injection (34, 57).

Indicators of subglacial deformation of the sandstone dikes and ridges include dikes deformed by nonsystematic folds, imbricate folds (inclined and recumbent), and reverse-faults [*SI Appendix*, Fig. S3; cf. ref. 59]; lobate, bulbous, and curved contacts with crystalline host rock [*SI Appendix*, Fig. S3*D*; (14)]; injectite sills with apophyses [*SI Appendix*, Fig. S6 *H* and *I*; cf. ref. 35]; ruptured pebbles [*SI Appendix*, Fig. S1*C*; (56–58, 60)]; and brecciated angular fragments of 1st-generation (purple) Tava within 2nd-generation (white) Tava injectites resulting from successive pulses of intrusion [*SI Appendix*, Fig. S3; (35)]. Deformation of sandstone ridges is represented by close-spaced grooved, striated shear surfaces [*SI Appendix*, Fig. S4 *B* and *C*; refs. 18 and 60], and imbricate faults/duplexes [*SI Appendix*, Fig. S4, e.g., refs. 61 and 62]. The scale, geometry, and form of structures developed in the Tava sandstone are dissimilar to brittle structures developed in Phanerozoic rocks of the Front Range (cf. refs. 16 and 35–37), in that fault planes and fold axes are independent of regional trends, and fold hinge zones lack cleavage: indications that folding occurred while the sediments were soft, prior to lithification and Phanerozoic tectonism.

Model for Snowball Subglacial Deposits and Tava Dike Injection during Meltwater Events. Taken together, Tava attributes are best understood as the product of glacial loading, fluid overpressure, sediment mobilization and emplacement, and deformation at the ice–bed interface in an evolving subglacial system, where sediment flux rates and transport modes vary dramatically over space and time (e.g., ref. 54). What is unique about the Tava subglacial system is that it formed when Laurentia was at an equatorial latitude, as demonstrated by robust ca. 719 Ma paleomagnetic constraints (43, 63). The data are consistent with the presence of large equatorial ice sheets in the interior of Laurentia during the Sturtian glaciation. Other evidence for Sturtian grounded ice and subglacial erosion on equatorial Laurentia exists in the Wasatch Mountains near Salt Lake City, Utah, where a possible glacial pavement in a U-shaped paleovalley has been described at the base of the Mineral Fork diamictite (64), although this interpretation was recently challenged (65).

The data presented herein document multiple pulses of Tava dike injection, which required the generation of meltwater and fluid overpressure. The ca. 690 Ma U-Pb hematite dates fall within the early to middle stages of the 717–661 Ma Sturtian glaciation (13, 63) and overlap with Cryogenian rifting on the western margin (63) and peak rift-related magmatism in Idaho (66), which is the closest known example of magmatism to the sample site (Fig. 4), Climate models agree that temperatures in the early stages of Snowball Earth would have been very cold, not conducive to much basal melting such that ice velocities were low (2). We propose that regional rift-related crustal thinning and magmatism increased the geothermal gradient, locally melted the ice sheet from below, and drove local hydrothermal circulation upon faults (Fig. 4) (cf. ref. 44) such as the ancestral Ute Pass Fault. The meltwater may have mobilized and concentrated sediment under the ice, leading to formation of subglacial channels (67), which were later deformed into sand ridges (58). Occasional pulses of fluid overpressure caused early episodes of Tava sand injection. Within sand ridges, the recumbent ptygmatic folding of dikes [Fig. 2 *A* and *B*; (35)] and ruptured pebbles [*SI Appendix*, Fig. S6 *H* and *I*; (56)] at dike margins provide evidence of subsequent glaciotectonic deformation due to ice–bed coupling with the overriding icesheet (58).

The ca. 660 Ma dates for the hematite-quartz veins overlap with Sturtian deglaciation (Fig. 4) (43, 59). During the latest stages of glaciation, seasonal supraglacial meltwater would have descended through moulins (6) or crevasses to the base of the icesheet, where, augmented by basal ice melt, it increased ice velocity and decreased friction (55). A further contribution may have come from groundwater exfiltration beneath the thinning ice sheet, a mechanism documented from analysis of contemporary satellite altimetry over Greenland and Iceland (74). The increase in water at the base of the ice sheet may have been the source of fluid overpressure for injection of light-colored, younger-generation Tava dikes and sills (Fig. 2 *C* and *D* and *SI Appendix*, Figs. S1*A*, S3, and S7*A*). Significantly, Tava sills indicate reduced "cryostatic" pressure (vertical overburden stress, i.e., ref. 51) that allowed propagation of hydrofractures along preexisting weaknesses (cf. refs. 51 and 57) such as isoclinal folds limbs, shear planes [*SI Appendix*, Fig. S3;

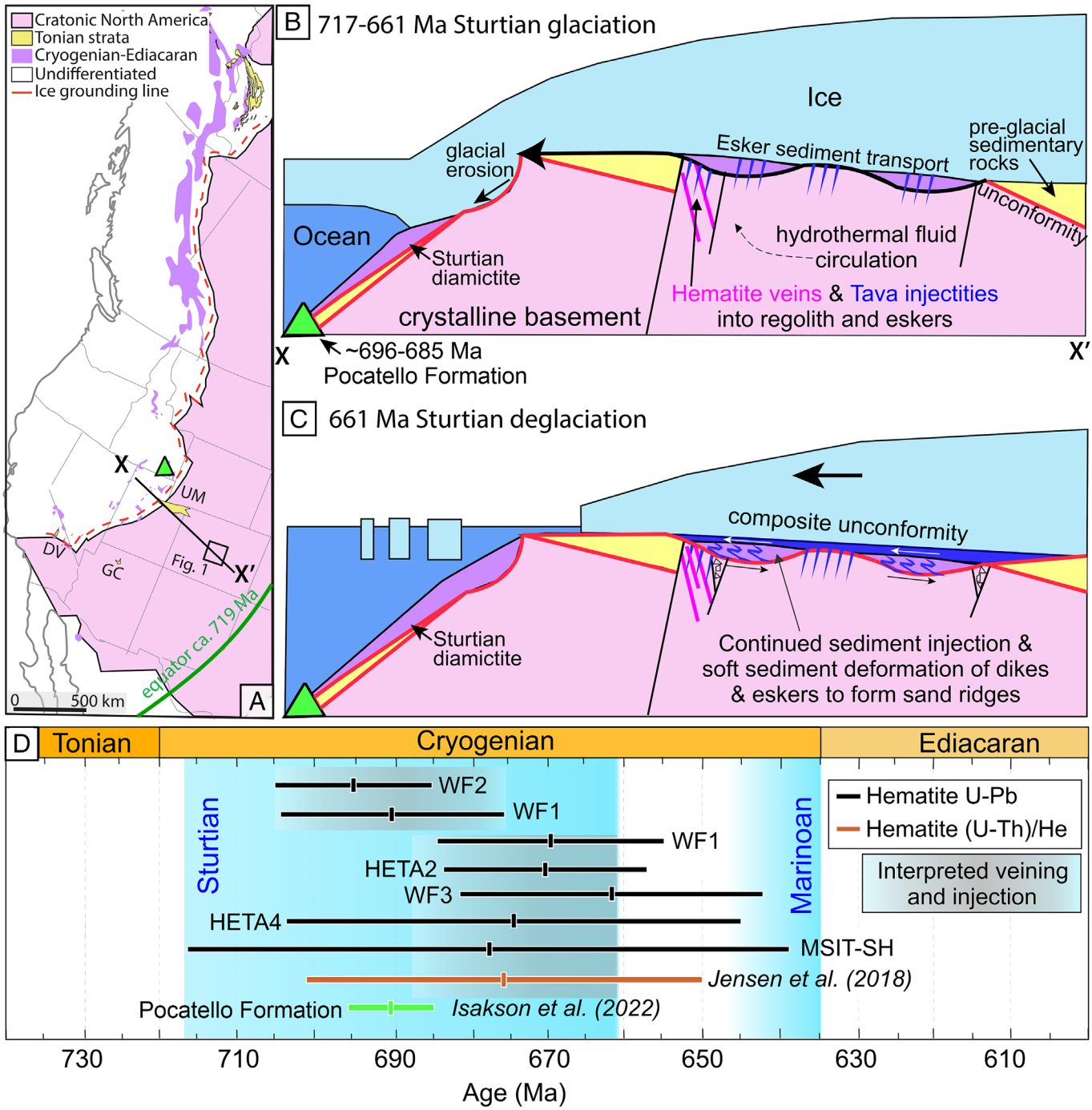

Fig. 4. Relationship between glaciation, deglaciation, and hematite U-Pb geochronology. (*A*) Simplified map of the western United States that shows the location of the field area in Fig. 1 and the distribution of Neoproterozoic strata across the western United States, modified from ref. 14. DV–Death Valley, GC–Grand Canyon, UM–Uinta Mountains. Position of ice-grounding line from ref. 43 and references therein. Position of the equator is calculated from paleomagnetic data on the ca. 719 Ma Franklin large igneous province (68). (*B*) Schematic cross-section of subglacial environments during the Sturtian glaciation from 717-661 Ma, which coincided both with rifting and glaciation. Hematite-quartz veins and Tava sedimentary injectites localized upon ancestral faults. Evidence for grounded ice and subglacial erosion is present in the Wasatch Mountains near Salt Lake City at the base of the Sturtian Mineral Fork diamictite (69; cf. ref. 70). Farther to the west in Utah and Nevada, there is no evidence for ice-grounding but instead for stratified ice rafted debris and flow tills ((43), and references therein). Rift-related magmatism is recorded in the Pocatello Formation, which has yielded dates between 696-685 Ma (71) during glaciation of Rodinia. Position of the cross-section X-X′ is shown in *A*. (*C*) Schematic cross-section of subglacial environments during the Sturtian deglaciation at 661 Ma (44, 72). Tava injections continue due to hydraulic overpressure (66); injectites and preglacial regolith undergo soft-sediment deformation beneath the icesheet during deglaciation. (*D*) Summary of geochronological results from this study in the context of the Cryogenian glaciations (44, 72, 73), previous hematite (U-Th)/He results (19), and dated magmatism in the Pocatello Formation (71).

(13)], basement fractures, and the earlier injectite array (Fig. 2*D*). In the presence of interstitial and basal water, the warming ice likely sped up, sculpting underlying sediment into ridges, with lubrication at the bed driving glacio-tectonism. Glacial isostatic rebound may have induced seismicity along the ancestral Ute Pass Fault or other structures (75), causing further sand injection during deglaciation.

We suggest that the hydrothermal fluids from which the hematite-quartz veins were precipitated at temperatures of ~210 to 230 °C (19) were sourced from basinal brines (e.g., ref. 44) and were

either highly oxidizing (68) or interacted with oxidized glacial meltwater derived from atmospheric oxygen transported through bubbles in glacial ice (68–71). Generally, atmospheric oxygen should have been highest at the start of glaciation and decreased during the Sturtian glaciation as organic carbon burial was diminished and reduced metals in ocean ridges and the crust consumed oxidants (72).

A potential analog for localization of fluids and geothermal heat along crustal structures may be found beneath the contemporary Antarctic ice sheet, where ice thicknesses can exceed 3,000 m. Although specific sites of geothermal activity are difficult to detect (76) or model (77), there is a portion of glaciated Antarctica in the Ross Embayment that is underlain by rift-related faults bordering sediment-filled basins (78). It offers an example of a contemporary system wherein iron-mineralizing fluids from depth could circulate in overpressured, fluidized supracrustal sediment along a narrow interface with weathered crystalline bedrock. Recent airborne and ice-sheet-based geophysical data collected across the Siple Coast grounding zone in the Ross Embayment reveal the presence of unconsolidated sedimentary fill in narrow structural basins, bounded by broad bedrock highs (78), with integrated glaciofluvial drainages that undergo repeated meltwater discharge events beneath grounded ice (79). When the Antarctic ice sheet was at maximum extent (80), the active basin-bounding faults beneath Siple Coast were >400 m and up to >1,000 m from the shelf-slope break, in a terrestrial subglacial setting. In these environments, deep groundwater and brines are present within subice sediments, functioning as a dynamic hydrological system that is responsive to variations in ice-sheet thickness, drawing basal meltwater downward when ice sheets are at maximum extent, and releasing groundwater when ice sheets retreat (81). Broad, flat-topped basement highs in the Ross Embayment represent paleoland surfaces (e.g., ref. 82), with regolith cored at one location by the Deep Sea Drilling Program (83). The basement highs, now subsided below sea-level (78, 84), display similar areal extent and degree of faulting/ fracturing as observed in the Colorado Front Range example (13). There is extensive preservation in Antarctica of preglacial landscapes beneath the ice sheets, despite the ≥30 My of existence of continental ice (73, 85).

Limited Basement Erosion in the Laurentian Continental Interior by the Snowball Ice Sheets. The relationships between the Tava injectites and crystalline basement (Fig. 2 *A* and *B* and *SI Appendix*, Fig. S7 *C* and *D*) support near-surface sand injection into a pre-Snowball regolith developed in exposed Proterozoic basement (14). Abundant local, crystalline-basement-derived detrital zircon (19–21) within the injectites indicates that the local basement was exposed at the surface and weathered prior to sand injection, and hence prior to the Sturtian glaciation for the climate conditions appropriate for basement weathering. The <3 km conditions for hematite precipitation in the hematite-quartz veins that mutually crosscut the Tava are consistent with the geologic evidence for shallow Tava emplacement. The zone of Tava dike injection is composed of chemically weathered granite (*SI Appendix*, Fig. S7) with semispherical bodies of intact granite that are interpreted as corestones (32, 86). This zone lacks characteristics indicative of mechanical scouring associated with substantial glacial erosion. Rather, the evidence for a pre-Snowball regolith supports limited basement denudation during Snowball Earth.

Low erosion across continental interiors by ice sheets is supported by the Cenozoic glaciations. For example, modeling suggests that less than 200 m of glacial erosion has occurred across much of the Antarctic interior (47, 87), bedrock erosion surfaces in East Antarctica were essentially uneroded during the Cenozoic glaciations (88), and plants in Arctic Canada that were entombed by ice caps have been re-exposed in their original growth positions (89). Collectively, the evidence supports exposure and weathering of the crystalline basement in the Laurentian continental interior of Colorado to form the Great Unconformity paleoland surface prior to the Sturtian glaciation, and minimal bedrock erosion caused by the Snowball ice sheets.

Materials and Methods

Hematite U-Pb Analysis and Data Reduction. One-inch round polished blocks were imaged via reflected light microscopy to inspect relationships between Tava and hematite at the microscale and screen hematite grains appropriate in size and morphology for U-Pb dating. LA–ICP–MS U–Pb and trace element data were collected at the CU TRaIL (Thermochronology Research and Instrumentation Lab at the University of Colorado, Boulder) over two analytical sessions using an ESI NWR193 excimer laser system attached to an Agilent 7900 ICP-MS. To assess the repeatability of hematite U-Pb measurements, one sample (HETA2) was also dated at the USGS Denver, using a 193 nm RESOlution-LR excimer laser coupled with an Agilent 8900 ICP-MS/MS. Analytical conditions for hematite U-Pb data acquisition broadly follow those outlined in refs. 31 and 90, which includes a spot size of 35 to 60 μm depending on sample grain sizes, repetition rate of 10 Hz, fluence of 3.5 Jcm^{-2}, 40 s ablation duration and a 30 s gas background. Measured isotopes included ^{57}Fe, ^{204}Pb, ^{206}Pb, ^{207}Pb, ^{208}Pb, ^{232}Th, and ^{238}U for a total integration time of 0.246 s. A recently developed synthetic hematite (HFO) was used as the primary reference material (31), with 91500, Plešovice, and either Temora-2 or RAK-17 zircons ran as secondary reference materials for quality control, whereby 91500 was the primary reference material for determining zircon secondary dates. No certified secondary hematite reference materials exist; however, in-house secondary hematite standards were run for further quality control. NIST 610 and 612 were also analyzed as reference materials for obtaining accurate U-Th-Pb trace element data. Analytical runs consisted of 3 to 4 HFO measurements, followed by two of each zircon and one of each NIST followed by 15 unknowns. U-Pb data were reduced using IOLITE v.4 and presented in IsoplotR. LA-ICP-MS pits were imaged using a KLA Zeta-20 optical profilometer.

Outcrop Imagery. Outcrop imagery was collected by a DJI Mavic 2 Pro drone at sites characterized during field studies over many years. Flights were programmed and executed via the photogrammetry tool in the UgCS mission planning software. Nadir images were collected along parallel flight lines such that vertical (along-line) overlap between consecutive images was 70% and horizontal overlap was 60%. Effective ground resolution was <1.5 cm/px at both Crystola and Manitou Springs. Drone imagery was used for photogrammetric reconstruction of outcrop topography in Agisoft Metashape. Three-dimensional topographic models permitted orthoprojection of imagery onto arbitrary planes (e.g., *SI Appendix*, Fig S4). Nine cairns at Manitou Springs served as ground control points (GCPs), which were surveyed with a Bad Elf Surveyor Global Navigation Satellite System unit and subsequently differentially postprocessed with RTKlib. No GCPs were utilized at Crystola.

Data, Materials, and Software Availability. All study data are included in the article and/or *SI Appendix*.

ACKNOWLEDGMENTS. This research was supported by NSF Division of Earth Sciences Grants EAR-1822119, EAR-1920648, and EAR-2203532 to R.M. Flowers. K. Kellogg (USGS) informed C.S. Siddoway about the Williams Fork locality, and White River National Forest authorized sampling in the Ptarmigan Peak Wilderness Area. B. Levenstein, P. Martin, and B. Peak aided in identification of hematite-Tava relationships at the Manitou Springs location. Thanks to Jay M. Thompson for U-Pb dating a hematite sample at the USGS Denver facilities and facilitating interlaboratory comparison. We are grateful to J. Jensen, A. Ault, and P. Reiners for valuable discussions. Sincere thanks to J.L. Kirschvink and two anonymous reviewers who provided thorough, constructive and thoughtful reviews which improved this contribution.

Author affiliations: [a]Department of Geological Sciences, University of Colorado Boulder, Boulder, CO 80309; [b]Department of Geology, Colorado College, Colorado Springs, CO 80946; [c]Earth Science Department, University of California–Santa Barbara, Santa Barbara, CA 93106; and [d]Department of Earth and Planetary Science, University of California–Berkeley, Berkeley, CA 94720

1. R. T. Pierrehumbert, D. S. Abbot, A. Voigt, D. Koll, Climate of the neoproterozoic. *Annu. Rev. Earth Planet. Sci.* **39**, 417–460 (2011).
2. D. S. Abbot *et al.*, Robust elements of Snowball Earth atmospheric circulation and oases for life. *J. Geophys. Res. Atmos.* **118**, 6017–6027 (2013).
3. R. C. Ewing *et al.*, New constraints on equatorial temperatures during a Late Neoproterozoic Snowball Earth glaciation. *Earth. Plan. Sci. Lett.* **406**, 110–122 (2014).
4. D. Benn *et al.*, Orbitally forced ice sheet fluctuations during the Marinoan Snowball Earth glaciation. *Nat. Geosci.* **8**, 704–707 (2015).
5. J. R. Creveling, J. X. Mitrovica, The sea–level fingerprint of a Snowball Earth deglaciation. *Earth. Plan. Sci. Lett.* **399**, 74–85 (2014).
6. P. F. Hoffman *et al.*, Snowball Earth climate dynamics and Cryogenian geology-geobiology. *Sci. Adv.* **3**, e1600983 (2017).
7. M. D. Crittendon, N. Christie-Blick, P. K. Link, Evidence for two pulses of glaciation during the late Proterozoic in northern Utah and southeastern Idaho. *GSA Bull.* **94**, 437–450 (1983).
8. G. H. Eisbacher, Late Proterozoic rifting, glacial sedimentation, and sedimentary cycles in the light of Windermere deposition, western Canada. *Palaeogeogr. Palaeoclimatol. Palaeoecol.* **51**, 231–254 (1985).
9. J. M. G. Miller, Glacial and syntectonic sedimentation: The upper proterozoic kingston peak formation, southern panamint range, eastern California. *GSA Bull.* **96**, 1537–1553 (1985).
10. S. V. Sobolev, M. Brown, Surface erosion events controlled the evolution of plate tectonics on Earth. *Nature* **570**, 52–57 (2019).
11. C. B. Keller *et al.*, Neoproterozoic glacial origin of the Great Unconformity. *Proc. Natl. Acad. Sci. U.S.A.* **116**, 1136–1145 (2019).
12. K. T. McDannell, C. B. Keller, W. R. Guenthner, P. K. Zeitler, D. L. Shuster, Thermochronologic constraints on the origin of the Great Unconformity. *Proc. Natl. Acad. Sci. U.S.A.* **119**, e2118682119 (2022).
13. C. S. Siddoway, G. Palladino, G. Prosser, D. Freedman, W. C. Duckworth, "Basement-hosted sand injectites: Use of field examples to advance understanding of hydrocarbon reservoirs in fractured basement rocks" in *Subsurface Sand Remobilization and Injection*, , M. Bowman, Ed. (Geological Society, London, Special Publications, 2019), vol. 493, pp. 215–233.
14. R. M. Flowers, F. A. Macdonald, C. S. Siddoway, R. Havranek, Diachronous development of the great unconformity prior to Snowball Earth. *Proc. Natl. Acad. Sci. U.S.A.* **117**, 10172–10180 (2020).
15. J. Temple, R. Madole, J. W. Keller, D. Martin, *Geologic Map of the Mount Deception Quadrangle, Teller and El Paso Counties* (Open–File Report OF–07–07, Colorado Geological Survey, Colorado, 2007), scale 1:24,000.
16. J. W. Keller *et al.*, "Geologic map of the Manitou springs quadrangle, El Paso County, Colorado" (Open–File report 03–19, Colorado Geological Survey, Denver, CO, 2005), Map at 1: 24 000 and text.
17. R. A. Wobus, G. R. Scott, "Reconnaissance geologic map of the Woodland Park quadrangle, Teller County" (U.S. Geological Survey, Colorado, 1977), Miscellaneous Field Studies Map MF–842, scale 1:24,000.
18. R. J. H. Jolly, L. Lonergan, Mechanisms and controls on the formation of sand intrusions. *J. Geol. Soc.* **159**, 605–617 (2002).
19. J. L. Jensen *et al.*, Single-crystal hematite (U–Th)/He dates and fluid inclusions document widespread Cryogenian sand injection in crystalline basement. *Earth. Plan. Sci. Lett.* **500**, 145–155 (2018).
20. C. S. Siddoway, G. E. Gehrels, Basement-hosted sandstone injectites of Colorado: A vestige of the Neoproterozoic revealed through detrital zircon provenance analysis. *Lithosphere* **6**, 403–408 (2014).
21. L. M. Fonseca Teixeira *et al.*, Tracking quartz and zircon provenance in sedimentary rocks using Ti distributions: Unlocking the volcanic–plutonic connection in old igneous systems. *Earth Planet. Sci. Lett.* **683**, 118906 (2024), 10.1016/j.epsl.2024.118906.K.
22. K. A. Farley, R. M. Flowers, (U-Th)/Ne and multidomain (U-Th)/He systematics of a hydrothermal hematite from eastern Grand Canyon. *Earth. Plan. Sci. Lett* **359–360**, 131–140 (2012).
23. C. L. Ciobanu, B. P. Wade, N. J. Cook, M. A. Schmidt, D. Giles, Uranium–bearing hematite from the Olympic Dam Cu–U– Au deposit, South Australia: A geochemical tracer and reconnaissance Pb–Pb geochronometer. *Precamb. Res.* **238**, 129–147 (2013).
24. E. I. Ilton *et al.*, Pentavalent Uranium Incorporated in the Structure of Proterozoic Hematite. *Environ. Sci. Tech.* **56**, 11857–11864 (2022).
25. L. Courtney-Davies *et al.*, A multi–technique evaluation of hydrothermal hematite U-Pb isotope systematics: Implications for ore deposit geochronology. *Chem. Geol.* **513**, 54–72 (2019).
26. L. Courtney-Davies *et al.*, Hematite geochronology reveals a tectonic trigger for iron ore mineralization during Nuna breakup. *Geology* **50**, 1318–1323 (2022).
27. A. K. Ault, Hematite fault rock thermochronometry and textures inform fault zone processes. *J. Struct. Geo.* **133**, 104002 (2020).
28. E. B. Watson, D. J. Cherniak, C. I. O. Nichols, B. P. Weiss, Pb diffusion in magnetite: Dating magnetite crystallization and the timing of remanent magnetization in banded iron formation. *Chem. Geol.* **640**, 121748 (2023).
29. L. Courtney-Davies *et al.*, Opening the magmatic–hydrothermal window: High–precision U–Pb geochronology of the Mesoproterozoic Olympic Dam Fe–oxide–Cu–U–Au–Ag deposit, South Australia. *Econ. Geol.* **115**, 1855–1870 (2020).
30. L. Courtney-Davies *et al.*, A synthetic haematite reference material for LA–ICP–MS U-Pb geochronology and application to iron oxide–Cu–Au systems. *Geostand. Geoanal. Res.* **45**, 143–159 (2021).
31. G. F. Carpenter, "Geology of the Sutherland Creek area, Manitou Embayment, Colorado, with emphasis on petrography as evidence for the Sawatch Sandstone source of the sandstone dikes," MSc thesis, Louisiana State University, Baton Rouge, LA, 1967), vol. 109.
32. C. S. Siddoway, P. Myrow, E. Fitz Díaz, "Strata, structures and enduring enigmas: A 125th Anniversary appraisal of Colorado Springs geology" in *Classic Concepts and New Directions: Exploring 125 Years of GSA Discoveries in the Rocky Mountain Region*, L. Abbott, G. S. Hancock, Eds. (Geological Society of America Field Guides, 2013), vol. 33.
33. M. Deynoux, J. F. Ghienne, Late Ordovician glacial pavements revisited: A reappraisal of the origin of striated surfaces. *Terra. Nova.* **16**, 95–101 (2004).
34. V. von Brunn, C. J. Talbot, Formation and deformation of subglacial intrusive clastic sheets in the Dwyka formation of northern Natal, South Africa. *J. Sed. Pet.* **56**, 35–44 (1986).
35. C. E. Chapin, S. A. Kelley, S. M. Cather, The Rocky Mountain Front, southwestern USA. *Geosphere.* **10**, 1043–1060 (2014).
36. C. F. Kluth, "Comparison of the location and structure of the late paleozoic and late cretaceous–Early tertiary front range uplift" in *Geologic history of the Colorado Front Range: Denver*, D. W. Bolyard, S. A. Sonnenberg, Eds. (Rocky Mountain Association of Geologists, Colorado, 1997), pp. 31–42.
37. K. S. Kellogg, How far does the Williams Range Thrust near Dillon, Colorado, overhang Cretaceous rocks? *Geolog. Soc Am.* **38**, 32 (2006), Abstracts with Programs.
38. R. L. Landman, R. M. Flowers, U-Th)/He thermochronologic constraints on the evolution of the northern Rio Grande Rift, Gore Range, Colorado, and implications for rift propagation models. *Geosphere* **9**, 170–187 (2013).
39. G. R. Scott, *Geology of the Kassler quadrangle, Jefferson and Douglas Counties* (Colorado, US Government Printing Office, 1963).
40. J. Dockal, Sandstone dikes within the Arapaho Pass Fault, Indian Peaks Wilderness, Boulder and Grand counties. *Colorado. Mt. Geol.* **42**, 143–158 (2005).
41. W. Premo, "SHRIMP U-Pb zircon ages for Big Creek gneiss, Wyoming and Boulder Creek batholith, Colorado: Implications for timing of Paleoproterozoic accretion of the northern Colorado province" (Rocky Mountain Geology, University of Wyoming, Colorado, WY, 2000), vol. 35, pp. 31–50.
42. F. A. Macdonald, W. A. Yonkee, R. M. Flowers, N. L. Swanson-Hysell, "Neoproterozoic of laurentia" in *Laurentia: Turning Points in the Evolution of a Continent*, S. J. Whitmeyer, M. L. Williams, D. A. KelLett, Eds. (Basil Tikoff, 2023).
43. A. D. Rooney, J. V. Strauss, A. D. Brandon, F. A. Macdonald, A Cryogenian chronology: Two long-lasting synchronous Neoproterozoic glaciations. *Geology* **43**, 459–462 (2015).
44. M. Steele–MacInnis, J. Ridley, P. Lecumberri-Sanchez, T. Schlegel, C. A. Heinrich, Application of low-temperature microthermometric data for interpreting multicomponent fluid inclusion compositions. *Earth Sci. Rev.* **159**, 14–35 (2016).
45. R. Jonk, J. Kelly, J. Parnell, The origin and tectonic significance of Lewisian-and Torridonian–hosted clastic dykes near Gairloch, NW Scotland. *Scott. J. Geol.* **40**, 123–130 (2004).
46. M. Vigorito, A. Hurst, J. Cartwright, A. Scott, Regional- scale subsurface sand remobilization: Geometry and architecture. *J. Geol. Soc. Lond.* **165**, 609–612 (2008).
47. E. Ravier *et al.*, Sedimentological and deformational criteria for discriminating subglaciofluvial deposits from subaqueous ice-contact fan deposits: A Pleistocene example (Ireland). *Sedimentol.* **61**, 1382–1410 (2014).
48. G. E. Williams, P. W. Schmidt, G. M. Young, Strongly seasonal Proterozoic glacial climate in low palaeolatitudes: Radically different climate system on the pre-Ediacaran Earth. *Geosci. Front.* **7**, 555–571 (2016).
49. M. Denis, J. F. Buoncristiani, M. Konaté, M. Guiraud, The origin and glaciodynamic significance of sandstone ridge networks from the Hirnantian glaciation of the Djado Basin (Niger). *Sedimentol.* **54**, 1225–1243 (2007).
50. G. Douillet *et al.*, Late Ordovician tunnel valleys in southern Jordan. *Geol. Soc. London. Sp. Publ.* **368** (2012).
51. E. Phillips, J. Everest, H. Reeves, Micromorphological evidence for subglacial multiphase sedimentation and deformation during overpressurized fluid flow associated with hydrofracturing. *Boreas* **42**, 395–427 (2013).
52. E. Ravier, J. F. Buoncristiani, J. Menzies, M. Guiraud, E. Portier, Clastic injection dynamics during ice front oscillations: A case example from Sólheimajökull (Iceland). *Sed. Geol.* **323**, 92–109 (2015).
53. J. Menzies, J. J. M. van der Meer, W. W. Shilts, "Subglacial processes and sediments" in *Past Glacial Environments*, J. Menzies, J. J. M. van der Meer, Eds. (Elsevier, ed. 2, 2018), pp. 105–158.
54. A. Hurst, A. Scott, M. Vigorito, Physical characteristics of sand injectites. *Earth. Sci. Rev.* **106**, 215–246 (2011).
55. E. Ravier *et al.*, Does porewater or meltwater control tunnel valley genesis? Case studies from the Hirnantian of Morocco. *Palaeogeog. Palaeoclimat. Palaeoecol.* **418**, 359–376 (2015).
56. J. J. M. van der Meer, K. H. Kjær, J. Krüger, J. Rabassa, A. A. Kilfeather, Under pressure: Clastic dykes in glacial settings. *Quat. Sci. Rev.* **28**, 1–13 (2008).
57. E. Ravier, Physical characteristics of hydrofracture systems and their fills in glacial sediments. *Sed. Geol.* **463**, 106593 (2024).
58. E. Phillips, D. J. A. Evans, Synsedimentary glacitectonic deformation within a glacilacustrine–esker sequence, Teesdale, Northern England. *Proc. Geolog. Assoc.* **130**, 624–649 (2019).
59. A. D. Rooney, C. Yang, D. J. Condon, M. Zhu, F. A. Macdonald, U-Pb and Re-Os geochronology tracks stratigraphic condensation in the Sturtian Snowball Earth aftermath. *Geology* **48**, 625–629 (2020).
60. B. Woronko, S. Belzyt, L. Bujak, M. Pisarska-Jamroży, Glaciotectonically deformed glaciofluvial sediments with ruptured pebbles (the Koczery study site, E Poland). *Bull. Geolog. Soc. Finland* **90**, 145–159 (2018).
61. S. A. S. Pedersen, Superimposed deformation in glaciotectonics. *Bull. Geol. Soc. Den.* **46**, 125–144 (2000).
62. S. A. S. Pederson, Architecture of glaciotectonic complexes. *Geosciences* **4**, 269–296 (2014).
63. F. A. Macdonald, N. L. Swanson-Hysell, The Franklin large igneous province and Snowball earth initiation. *Elements* **19**, 296–301 (2023).
64. N. Christie–Blick, "Neoproterozuic sedimentation and tectonics in West-Central Utah" in *Proterozoic to Recent Stratigraphy, Tectonics and Volcanology*, P. K. Link, B. J. Kowallis, Eds. (Brigham Young University Geology Studies, Utah, Nevada, Southern Idaho and Central Mexico, 1997), vol. 42, pp. 1–30.
65. T. M. Vandyk *et al.*, Reassessing classic evidence for warm–based Cryogenian ice on the western Laurentian margin: The "striated pavement" of the Mineral Fork Formation, USA. *Precamb. Res.* **363**, 106345 (2021).
66. V. H. Isakson, M. D. Schmitz, C. M. Dehler, F. A. Macdonald, W. A. Yonkee, A robust age model for the Cryogenian Pocatello formation of southeastern Idaho (northwestern USA) from tandem in situ and isotope dilution U-Pb dating of volcanic tuffs and epiclastic detrital zircons. *Geosphere* **18**, 825–849 (2022).
67. E. Ravier, J. F. Buoncristiani, "Chapter 12–Glaciohydrogeology" in *Past Glacial Environments*, J. Menzies, J. J. M. van der Meer, Eds. (Elsevier, ed. 2, 2018), pp. 431–466.
68. J. Mikucki *et al.*, Deep groundwater and potential subsurface habitats beneath an Antarctic dry valley. *Nat. Commun.* **6**, 6831 (2015).
69. P. Glynn, C. Voss, A. M. Provost, "Deep penetration of oxygenated meltwaters from warm based icesheets into the fennoscandian shield" in *Technical Summary and Proceedings* (The NEA Co-ordinating Group on Site Evaluation and Design Experiments for Radioactive Waste Disposal (SEDE), Swedish Nuclear Fuel and Waste management Company (SKB), Borgholm, Sweden, 1997), pp. A17–A18.
70. H. Craig, R. A. Wharton Jr., C. P. Mckay, Oxygen supersaturation in ice-covered antarctic lakes: Biological versus physical contributions. *Science* **255**, 318–321 (1992).
71. C. P. McKay, K. P. Hand, P. T. Doran, D. T. Andersen, J. C. Priscu, Clathrate formation and the fate of noble and biologically useful gases in Lake Vostok, Antarctica. *Geophys. Res. Lett.* **30**, 1702 (2003).
72. G. Le Hir, Y. Goddéris, Y. Donnadieu, G. Ramstein, A geochemical modelling study of the evolution of the chemical composition of seawater linked to a "Snowball" glaciation. *Biogeosci.* **5**, 253–267 (2008).

73. S. S. R. Jamieson *et al.*, An ancient river landscape preserved beneath the East Antarctic Ice Sheet. *Nat. Commun.* **14**, 6507 (2023).
74. A. A. Robel, S. J. Sim, C. Meyer, M. R. Siegfried, C. D. Gustafson, Contemporary ice sheet thinning drives subglacial groundwater exfiltration with potential feedbacks on glacier flow. *Sci. Adv.* **9**, 33 (2023).
75. I. S. Stewart, J. Sauber, J. Rose, Glacio-seismotectonics: Ice sheets, crustal deformation and seismicity. *Quat. Sci. Rev.* **19**, 1367–1389 (2000).
76. C. B. Begeman, S. M. Tulaczyk, A. T. Fisher, A. T, Spatially variable geothermal heat flux in West Antarctica: Evidence and implications. *Geophys. Res. Lett.* **44**, 9823–9832 (2017).
77. A. Reading *et al.*, Geothermal heat flow of Antarctica with implications for its tectonics and ice sheets. *Nat. Rev. Earth. Env.* **3**, 814–831 (2022).
78. M. Tankersley, H. Horgan, C. Siddoway, F. Caratori Tontini, K. Tinto, Basement topography and sediment thickness beneath Antarctica's Ross Ice Shelf. *Geophys. Res. Lett.* **49**, 10 (2022).
79. H. Horgan *et al.*, *Subglacial Drainage across Kamb Ice Stream's Grounding Zone, West Antarctica* (EGU General Assembly, Vienna, Austria, 2023), **vol. 1820**.
80. N. R. Golledge, C. J. Fogwill, A. N. Macintosh, K. M. Buckley, Dynamics of the last glacial maximum Antarctic ice-sheet and its response to ocean forcing. *Proc. Natl. Acad. Sci. U.S.A.* **109**, 16052–16056 (2012).
81. C. D. Gustafson *et al.*, A dynamic saline groundwater system mapped beneath an Antarctic ice stream. *Science* **376**, 640–644 (2022).
82. L. De Santis, J. B. Anderson, G. Brancolini, I. Zayatz, "Seismic record of late Oligocene through Miocene glaciation on the central and eastern continental shelf of the Ross Sea" in *Geology and Seismic Stratigraphy of the Antarctic Margin*, A. K. Cooper, P. F. Barker, G. Brancolini, Eds. (Antarctic research series, American Geophysical Union, 1995), pp. 235–260.
83. A. Ford, P. J. Barrett, *Basement rocks of the south-central Ross Sea, site 270, DSDP leg 28* (Texas A & M University, Ocean Drilling Program, 1975).
84. D. Wilson, B. P. Luyendyk, Bedrock platforms within the Ross Embayment, West Antarctica: Hypotheses for ice sheet history, wave erosion, Cenozoic extension, and thermal subsidence. *Geochem. Geophys. Geosys.* **7** (2006).
85. S. S. R. Jamieson *et al.*, The glacial geomorphology of the Antarctic ice-sheet bed. *Antarct. Sci.* 26, 724–741.
86. P. M. Myrow, *Transgressive Stratigraphy and Depositional Framework of Cambrian Tidal Dune Deposits, Peerless Formation* (SEPM Special Publications, Central Colorado, 1998), **vol. 61**, pp. 143–154.
87. C. M. Carter *et al.*, Extensive palaeo-surfaces beneath the Evans–Rutford region of the West Antarctic Ice Sheet control modern and past ice flow. *The Cryosphere* **18**, 2277–2296 (2024).
88. G. J. G. Paxman *et al.*, Bedrock erosion surfaces record former East Antarctic Ice Sheet extent. *Geophys. Res. Lett.* **45**, 4114–4123 (2018).
89. S. L. Pendleton *et al.*, Rapidly receding Arctic Canada glaciers revealing landscapes continuously ice-covered for more than 40,000 years. *Nat. Commun.* **10**, 445 (2019).
90. L. Courtney-Davies *et al.*, A billion-year shift in the formation of Earth's largest ore deposits. *Proc. Natl. Acad. Sci. U.S.A.* **121**, e2405741121 (2024).